Hierarchical zeolites containing embedded $Cd_{0.2}Zn_{0.8}S$ as a photocatalyst for hydrogen production from seawater

COMMUNICATION

Hierarchical zeolites containing embedded $Cd_{0.2}Zn_{0.8}S$ as a photocatalyst for hydrogen production from seawater

Received 00th January 20xx,
Accepted 00th January 20xx

DOI: 10.1039/x0xx00000x

Yue Yuan[†a], Feng-Juan Wu[†a], Shi-Tian Xiao[†a], Yi-Tian Wang[†a], Zhi-Wen Yin[†a], Gustaaf Van Tendeloo[ab], Gang-Gang Chang[a], Ge Tian[a], Zhi-Yi Hu*[a], Si-Ming Wu*[a], Xiao-Yu Yang*[a]

Uncovering an efficient and stable photocatalytic system for seawater splitting is a highly desirable but challenging goal. Herein, $Cd_{0.2}Zn_{0.8}S$@Silicalite-1 (CZS@S-1) composites, in which CZS is embedded in the hierarchical zeolite S-1, were prepared and show remarkably high activity, stability and salt resistance in seawater.

Hydrogen production from seawater is an important strategy to generate energy from renewable resources.[1-5] From a global perspective, seawater is the most abundant natural resource and sun light is the greatest energy source. Therefore, photocatalytic splitting of seawater to produce H_2 has enormous potential.[6,7] However, this process is hindered by the various components in seawater including ions, microbes, etc.[3,6,8] Specifically, most photocatalysts developed for this purpose, thus far, are not resistant to electrochemical corrosion or surface fouling by these seawater constituents.[9-11] As a result, great interest exists in identifying methods to shield photocatalysts from problematic ions in seawater by incorporating them in porous corrosion resistant support materials like zeolites.[12,13]

Zeolites have a high chemical and thermal stability, along with advantageous features including unique pore structures, large specific surface areas and strong adsorption capacities.[14-16] Zeolites have been found to be very effective in seawater desalination due to their strong absorption of cations.[17-19] Although zeolites have an excellent ion selectivity, they typically possess micropores,[16] sizes that often limit their ability to embed nano-scale semiconductors.[20] In contrast, hierarchical zeolites not only possess inherent microporosity, they have mesoporosity or even macroporosity.[21] Approaches for the synthesis of hierarchical zeolites include removal of the framework atoms, templating methods, zeolitization of the preformed solids and silanization-based methods.[16,22] The range of pore sizes in hierarchical zeolites prepared using these methods induce a loss of absorbed nanoparticles such as nanocatalysts. This problem can be mitigated by introducing confinement features into the zeolites like hollow hierarchical structures comprised of microporous shells and macroporous cores. In addition to blocking the aggregation of nano-catalysts,[23] embedment in micropores in these types of hierarchical zeolites screen the catalysts from ions and substances in seawater that lead to corrosion and fouling.

Owing to its suitable band gap and high visible light absorption capacity, the semiconductor CZS is an efficient photocatalyst for solar H_2 production.[24,25] However, similar to CdS, pure CZS tends to aggregate to form large particles and a photocorrosion layer,[26,27] which leads to a low catalytic activity and stability. In this study, we prepared and investigated a new family of photocatalysts, CZS@S-1, containing different percentages of CZS, embedded in the hierarchical zeolite, S-1. The results demonstrate that 20% CZS@S-1 effectively photocatalysis H_2 production under UV-vis irradiation and possesses a high salt tolerance and stability.

The CZS@S-1 composites were prepared using the pathway shown in Fig. 1. In this route, 100 nm mesoporous silica (100 nm MS) was firstly synthesized. The lamellar closed pore zeolite S-1 was then prepared by a solid phase method with tetrapropylammonium hydroxide (TPAOH) as template and adding 1-octyl-3-methylimidazolium tetrafluoroborate ([OMIM]BF_4). Finally, one-step solvothermal reaction of S-1 with various amounts of $Cd(Ac)_2$, $Zn(Ac)_2$ and Na_2S produced the CZS@S-1 composites.[28]

[a] *State Key Laboratory of Advanced Technology for Materials Synthesis and Processing & School of Materials Science and Engineering & Nanostructure Research Centre & Chemical Engineering and Life Science School of Chemistry & Shenzhen Research Institute, Wuhan University of Technology, Wuhan, 430070, China.*
[b] *Electron Microscopy for Materials Science, University of Antwerp, Antwerpen B-2020, Belgium.*
† These authors contributed equally to this work.
Electronic Supplementary Information (ESI) available: [details of any supplementary information available should be included here]. See DOI: 10.1039/x0xx00000x

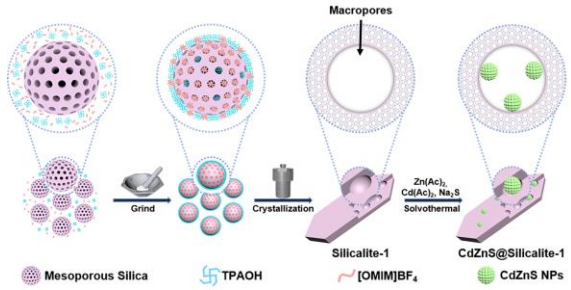

Fig. 1 Schematic illustration of the preparation of CZS@S-1.

CZS@S-1 composites were characterized by using SEM and EDX (Fig. S1, S2 and S3). SEM images shows that S-1 has a smooth surface, a hollow pore structure and thickness of about 300-600 nm. It indicates that the synthetic sequence result in the formation of molecular sieves with a lamellar closed pore structure. As shown in Fig. S1cd, unembedded CZS nanoparticles have a diameter of about 10-20 nm, and they have an obvious tendency to agglomerate to form massive structures. SEM images of CZS@S-1 composites (Fig. S1e-j) demostrate that inclusion in S-1 effectively reduces the agglomeration of CZS nanoparticles and improves their dispersion. As the content of CZS in CZS@S-1 composites is increases, the density of CZS nanoparticles on the S-1 surface increased gradually, but agglomeration of excess nanoparticles occurs when the content of CZS is high. EDX elemental mapping (Fig. S3) confirms that Si, O, Cd, Zn and S are uniformly distributed throughout this composite.

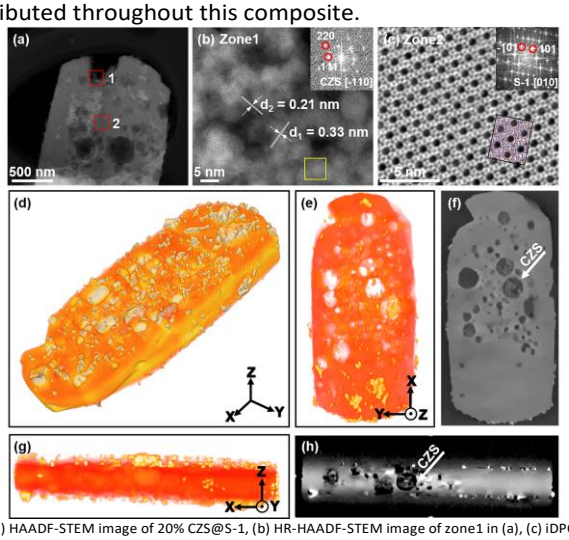

Fig. 2 (a) HAADF-STEM image of 20% CZS@S-1, (b) HR-HAADF-STEM image of zone1 in (a), (c) iDPC-STEM image of zone2 in (a), (d) 3D tomographic reconstruction, (e) 3D reconstruction along the z-axis, (f) HAADF-STEM image of orthoslices obtained from the 3D reconstruction (x-y plane, perpendicular to the z-axis) (g) 3D reconstruction along the y-axis, (h) HAADF-STEM image of an orthoslice obtained from the 3D reconstruction (x-z plane, perpendicular to the y-axis) of 20% CZS@S-1.

HAADF-STEM analysis (Fig. 2b) shows that the diameter of the CZS nanoparticles in 20% CZS@S-1 is about 10 nm. The HAADF-STEM images also reveal the existence of lattice fringes with lattice spacings of 0.33 and 0.21 nm assigned to the (111) and (220) crystal planes of CZS.[29] This observation suggests that the composite has a well-defined crystal structure. In addition, a clear five-member ring MFI structure can be seen by viewing the iDPC-STEM image of 20% CZS@S-1 in Fig. 2c, again indicating that the composite has high crystallinity.

To further study the hierarchical structure of S-1 and the distribution of CZS nanoparticles, a 3D tomographic reconstruction of 20% CZS@S-1 was performed. The internal section from the reconstructions (Fig. 2d-h and S4) shows that macropores are present inside the zeolite crystal, forming microporous shells and macroporous cores in hierarchical S-1. Moreover, the internal macropores are partially occupied by CZS nanoparticles, demonstrating again that CZS nanoparticles not only exist on the outer surface of S-1, but they are also distributed in the internal macropores.

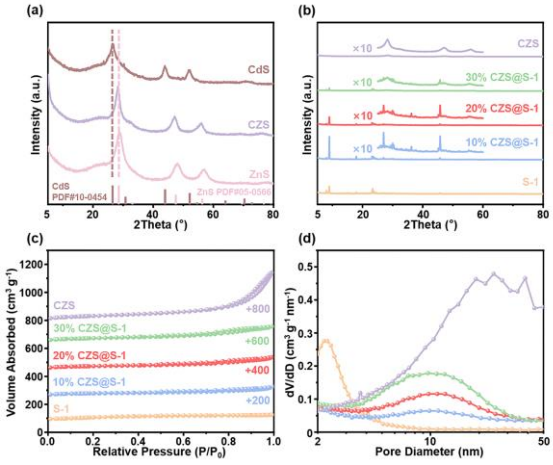

Fig. 3 (a) XRD patterns of $Cd_xZn_{1-x}S$, (b) XRD patterns , (c) N_2 adsorption/desorption isotherms and (d) corresponding pore size distributions of S-1, 10% CZS@S-1, 20% CZS@S-1, 30% CZS@S-1 and CZS.

The location of the diffraction peaks of CZS between those of ZnS and CdS indicate that CZS is a solid solution of $Cd_xZn_{1-x}S$ rather than a mixture of ZnS and CdS (Fig. 3a).[28] XRD patterns of CZS@S-1 composites containing different weight percentages of CZS are displayed in Fig. 3b. The XRD pattern of S-1 alone indicates its the MFI structure.[30,31] In addition, strong characteristic peaks associated with S-1 and CZS and weak background noise in the XRD patterns indicate that the crystal structure of S-1 is not changed by in-situ embedding of the CZS.[32] With an increase of CZS composition, intensities of the CZS XRD peaks increase gradually, while S-1 XRD peaks gradually decrease, reflecting the two-phase composition of S-1 and CZS in these composites.

The composition and chemical states of S-1, 20% CZS@S-1 and CZS were elucidated using XPS. Compared with those in the spectrum of S-1 (Fig. S5cd), the peaks corresponding to Si 2p and O 1s in the spectrum 20% CZS@S-1 are both shifted towards lower binding energies.[33] Also, compared with those in the spectrum of CZS (Fig. S5ef and 4d), the peaks associated with Cd 3d, Zn 2p and S 2p in 20% CZS@S-1 all shift towards higher binding energies, which is plausibly because of the electrostatic interaction existing between the doping material and the substrate material.[34]

Specific surface areas and pore diameter distributions of the CZS@S-1 composites were determined by analysis of N_2 adsorption-desorption isotherms (Fig. 3cd and Table S1). Isotherms of all composites (Fig. 3c) belong to the type IV group, revealing that they have mesoporous structures.[35] Notably, CZS were found to contain mesoporous pores which might be a consequence of voids formed by aggregation of the

nanoparticles.[28] The specific surface areas of the CZS@S-1 composites fall between those of S-1 and CZS, and that they decrease at first and then remain unchanged with increases in the CZS content. This phenomenon could be caused by simultaneous growth of the CZS nanoparticles in the pores and on the surface of S-1. Specifically, when the CZS content is low, an increase in the CZS content leads to growth of CZS nanoparticles in pores which causes a decrease in the specific surface area of CZS@S-1. As the content of CZS increase, the growth of CZS nanoparticles in S-1 pores reaches saturation and the specific surface area plateaus.

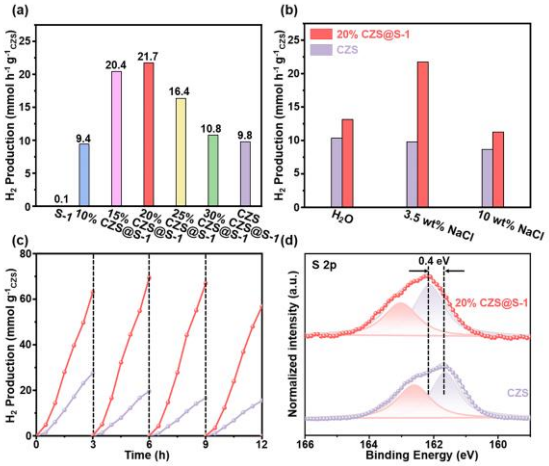

Fig. 4 (a) Photocatalytic H_2 production activities of S-1, 10% CZS@S-1, 15% CZS@S-1, 20% CZS@S-1, 25% CZS@S-1, 30% CZS@S-1 and CZS in simulated seawater, (b) Photocatalytic H_2 production activity of 20% CZS@S-1 and CZS in varying concentrations of aqueous NaCl, (c) Photocatalytic H_2 production promoted by 20% CZS@S-1 and CZS in simulated seawater during different time cycles, a certain amount of sacrificial agent is added during each cycle, and (d) XPS S 2p spectra of 20% CZS@S-1 and CZS.

The appearance of the characteristic peaks of five-membered ring MFI structure from FT-IR spectra (Fig. S6) of CZS@S-1 matches with XRD analysis that the MFI structure of S-1 is not changed by incorporation of CZS.[36,37] UV-vis DRS were collected on CZS@S-1 composites and CZS. CZS strongly absorbs light of $\lambda < 500$ nm (Fig. S7a), which correspond to its band gap of 2.68 eV based on the Tauc plot shown in Fig. S7b. In comparison, the CZS@S-1 composites have shorter wavelength absorption edges and wider band gaps. Also, as the CZS content increases, the absorption edge values of the composite first increases and then plateau, and the band gaps first decrease and then plateau. Photoelectrochemical measurements show that CZS@S-1 composites have lower transient photocurrent responses (Fig. S8a) and larger arc radius in EIS Nyquist plots (Fig. S8b) than does CZS, which is due to the decease of conductivity caused by the coating of S-1. The Mott-Schottky curves of CZS@S-1 show a slightly positive shift compared with those of CZS (Fig. S9). The calculated band position of CZS is shown in Fig S10.

The photocatalytic H_2 production activities of the CZS@S-1 composites containing different weight percentages of CZS were determined using UV-vis light irradiation along with Na_2S and Na_2SO_3 as sacrificial agents (Fig. 4a and Table S2). As shown in Fig. 4a, the photocatalytic H_2 evolution rate is negligible when S-1 is used as the photocatalyst, and CZS displays a finite but small (H_2 evolution 9.8 mmol $h^{-1}g^{-1}_{CZS}$) photocatalytic H_2 production activity. In comparison, CZS@S-1 composites containing an appropriate amount of CZS have significantly enhanced photocatalytic H_2 production activities. Specifically, as the CZS content increases from 10 to 20 wt%, the H_2 evolution rate reaches a maximum (21.7 mmol $h^{-1}g^{-1}_{CZS}$), which is 2.2-fold higher than that of pure CZS (Fig. 4a). A further increase in the content leads to a reduction in the photocatalytic activity, which may be caused by the agglomeration of excessive CZS. The photocatalytic H_2 production activities of 20% CZS@S-1 and CZS in different concentrations of aqueous NaCl show that the H_2 evolution rate of the CZS catalyzed process decreases with increasing NaCl concentration, whereas the H_2 evolution rate of the 20% CZS@S-1 catalyzed reaction first increases then decreases with increasing NaCl concentration (Fig.4b). In addition, the photocatalytic H_2 evolution rates of 20% CZS@S-1 are 1.3-, 2.2- and 1.3-fold higher in 0, 3.5 and 10 wt% of NaCl, respectively, than that of an equivalent per unit weight of CZS.

In addition to photocatalytic activity, stability is also an essential feature that needs to be evaluated. Stability tests were performed on the photocatalysts by measuring activities during 4 on-off cycles over a 12 h period(Fig. 4c and S11). The results (Fig. 4c) show that 20% CZS@S-1 in simulated seawater retains over 90% of its activity after 4 cycles, while CZS retains only 56% of the starting value. Also the morphology and structure of 20% CZS@S-1 display no obvious change after 12 h illumination in simulated seawater, which demonstates its excellent structural stability (Fig. S12 and S13).

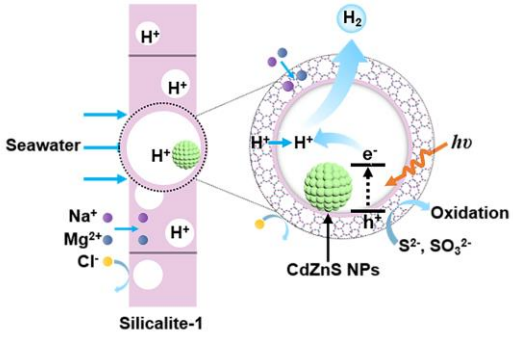

Fig. 5 The mechanism illustruction of CZS@S-1 for H_2 production from seawater.

Based on the above results, the possible mechanism of zeolite embedding photocatalyst for H_2 production from seawater is shown in Fig. 5. The as-prepared S-1 has good light transmittance and is of sheet structure, so light can penetrate it to reach the inside. Moreover, the hierarchical zeolite S-1 has a microporous shell and a macroporous core. The macropores in the internal structure serve as a platform for encapsulation of CZS to protect it from aggregation and photocorrosion. This is evidenced by the higher activity of CZS@S-1 over that of CZS in pure H_2O (Fig. 4b). In addition, the microporous shell blocks cations through an ion exchange process,[17-19] and thus photocorrosion of CZS and side reactions are greatly suppressed. Moreover, the acidic environment of the zeolite framework is beneficial for H_2 prodution.[38] Therefore, under light irradiation, photoelectrons generated on CZS react with the enriched H^+ in the zeolite structure to produce H_2, and the holes are consumed by sacrificial agents. As a result, the unique

CZS@S-1 structure leads to improved photocatalytic H_2 production activity and stability in seawater (Fig. S14, Fig 4c).

We proposed a simple method to prepare the hierarchical zeolite S-1 containing embedded nano-photocatalyst CZS. 20% CZS@S-1 possesses a higher photocatalytic activity and stability than CZS, owing to its hierarchical nature composed of a microporous surface and macroporous interior which respectively function to screen against corrosive ions and to disperse embedded photocatalyst molecules.

This work was supported by National Key Research and Development Program of China (2022YFB3805600, 2022YFB3805604, 2022YFB3806800), National Natural Science Foundation of China (22293020, 52103285, 21706199), National 111 project (B20002)，Program Fund of Non-Metallic Excellence and Innovation Center for Building Materials (2023TDA1-1)，Program for Changjiang Scholars and Innovative Research Team in University (IRT_15R52)，Guangdong Basic and Applied Basic Research Foundation (2022A1515010137, 2022A1515010504)，Shenzhen Science and Technology Program (GJHZ20210705143204014, JCYJ20210324142010029, KCXFZ20211020170006010), We thank the Nanostructure Research Centre (NRC) for the S/TEM work.

Conflicts of interest

There are no conflicts to declare.

Notes and references

1. H. Jin, X. Wang, C. Tang, A. Vasileff, L. Li, A. Slattery and S. Z. Qiao, *Adv. Mater.*, 2021, **33**, e2007508.
2. X. Y Yang, *Photo-Driven Seawater Splitting for Hydrogen Production*, Springer Singapore, Berlin, 2023.
3. H. Xie, Z. Zhao, T. Liu, Y. Wu, C. Lan, W. Jiang, L. Zhu, Y. Wang, D. Yang and Z. Shao, *Nature*, 2022, **612**, 673-678.
4. Y. X. Zhang, S. M. Wu, G. Tian, X. F. Zhao, L. Y. Wang, Y. X. Yin, L. Wu, Q. N. Li, Y. X. Zhang, J. S. Wu, C. Janiak, K. I. Ozoemena, M. Shalom and X. Y. Yang, *Chem. Eur. J.*, 2021, **27**, 14202-14208.
5. S. T. Xiao, R. Yin, L. Wu, S. M. Wu, G. Tian, M. Shalom, L. Y. Wang, Y. T. Wang, F. F. Pu, H. N. Barad, F. Wang and X. Y. Yang, *Nano Lett.*, 2023, DOI: 10.1021/acs.nanolett.3c00661.
6. S. M. Ji, H. Jun, J. S. Jang, H. C. Son, P. H. Borse and J. S. Lee, *J. Photoch. Photobio. A*, 2007, **189**, 141-144.
7. L. Zhang, Z. Wang and J. Qiu, *Adv. Mater.*, 2022, **34**, e2109321.
8. J. Zhang, W. Hu, S. Cao and L. Piao, *Nano Res.*, 2020, **13**, 2313-2322.
9. Y. Li, F. He, S. Peng, D. Gao, G. Lu and S. Li, *J. Mol. Catal. A: Chem.*, 2011, **341**, 71-76.
10. Y. Li, F. He, S. Peng, G. Lu and S. Li, *Int. J. Hydrogen Energy*, 2011, **36**, 10565-10573.
11. T. Song, P. Zhang, T. Wang, A. Ali and H. Zeng, *Nanoscale*, 2018, **10**, 2275-2284.
12. S. Anandan and M. Yoon, *J. Photoch. Photobio. C*, 2003, **4**, 5-18.
13. M. Kuronen, R. Harjula, J. Jernström, M. Vestenius and J. Lehto, *Phys. Chem. Chem. Phys.*, 2000, **2**, 2655-2659.
14. A. Corma and H. Garcia, *Chem. Commun.*, 2004, 1443-1459.
15. X. Deng, B. Qin, R. Liu, X. Qin, W. Dai, G. Wu, N. Guan, D. Ma and L. Li, *J. Am. Chem. Soc.*, 2021, **143**, 20898-20906.
16. D. P. Serrano, J. M. Escola and P. Pizarro, *Chem. Soc. Rev.*, 2013, **42**, 4004-4035.
17. S. F. Anis, R. Hashaikeh and N. Hilal, *Desalination*, 2019, **468**, 114077.
18. T. Wajima, T. Shimizu, T. Yamato and Y. Ikegami, *Toxicol. Environ. Chem.*, 2010, **92**, 21-26.
19. Z. Xue, Z. Li, J. Ma, X. Bai, Y. Kang, W. Hao and R. Li, *Desalination*, 2014, **341**, 10-18.
20. X. Y. Yang, L. H. Chen, Y. Li, J. C. Rooke, C. Sanchez and B. L. Su, *Chem. Soc. Rev.*, 2017, **46**, 481-558.
21. J. W. Liu, S. M. Wu, L. Y. Wang, G. Tian, Y. Qin, J. X. Wu, X. F. Zhao, Y. X. Zhang, G. G. Chang, L. Wu, Y. X. Zhang, Z. F. Li, C. Y. Guo, C. Janiak, S. Lenaerts and X. Y. Yang, *ChemCatChem*, 2020, **12**, 5364-5368.
22. M. H. Sun, J. Zhou, Z. Y. Hu, L. H. Chen, L. Y. Li, Y. D. Wang, Z. K. Xie, S. Turner, G. Van Tendeloo, T. Hasan and B. L. Su, *Matter*, 2020, **3**, 1226-1245.
23. S. M. Wu, X. Y. Yang and C. Janiak, *Angew. Chem. Int. Ed.*, 2019, **58**, 12340-12354.
24. M. Liu, L. Wang, G. Lu, X. Yao and L. Guo, *Energy Environ. Sci.*, 2011, **4**, 1372-1378.
25. Y. Wang, J. Wu, J. Zheng and R. Xu, *Catal. Sci. Technol.*, 2011, **1**, 940-947.
26. L. Yao, D. Wei, Y. Ni, D. Yan and C. Hu, *Nano Energy*, 2016, **26**, 248-256.
27. Y. Lu, X. Cheng, G. Tian, H. Zhao, L. He, J. Hu, S.-M. Wu, Y. Dong, G.-G. Chang, S. Lenaerts, S. Siffert, G. Van Tendeloo, Z.-F. Li, L.-L. Xu, X.-Y. Yang and B.-L. Su, *Nano Energy*, 2018, **47**, 8-17.
28. Y. Su, Z. Zhang, H. Liu and Y. Wang, *Appl. Catal. B.-Environ.*, 2017, **200**, 448-457.
29. F. Y. Tian, D. Hou, F. Tang, M. Deng, X. q. Qiao, Q. Zhang, T. Wu and D. S. Li, *J. Mater. Chem. A*, 2018, **6**, 17086-17094.
30. X. Zhuang, X. Chen, Y. Su, J. Luo, S. Feng, H. Zhou and Y. Wan, *J. Membr. Sci.*, 2016, **499**, 386-395.
31. Y. T. Wang, S. M. Wu, G. Q. Luo, G. Tian, B. J. Zeng, L. Y. Wang, S. T. Xiao, J. X. Wu, A. Wu, K. J. Wu, S. Lenaerts and X. Y. Yang, *Appl. Catal. A-GEN.*, 2023, **650**, 119016.
32. P. Yu, M. Cui, Q. Li, D. Wang, Z. Wang, M. Li and X. Li, *Appl. Catal. A-GEN.*, 2020, **608**, 117860.
33. Z. Li and Y. Zhu, *Appl. Surf. Sci.*, 2003, **211**, 315-320.
34. Y. Lei, Y. Zhang, Z. Li, S. Xu, J. Huang, K. Hoong Ng and Y. Lai, *Chem. Eng. J.*, 2021, **425**, 131478.
35. S. M. Wu, X. L. Liu, X. L. Lian, G. Tian, C. Janiak, Y. X. Zhang, Y. Lu, H. Z. Yu, J. Hu, H. Wei, H. Zhao, G. G. Chang, G. Van Tendeloo, L. Y. Wang, X. Y. Yang and B. L. Su, *Adv. Mater.*, 2018, **30**, 1802173.
36. R. Sabarish and G. Unnikrishnan, *J. Mol. Liq.*, 2018, **272**, 919-929.
37. S. T. Xiao, S. M. Wu, Y. Dong, J. W. Liu, L. Y. Wang, L. Wu, Y. X. Zhang, G. Tian, C. Janiak, M. Shalom, Y. T. Wang, Y. Z. Li, R. K. Jia, D. W. Bahnemann and X. Y. Yang, *Chem. Eng. J.*, 2020, **400**, 125909.
38. Q. M. Sun, N. Wang, R. S. Bai, Y. Hui, T. J. Zhang, D. A. Do, P. Zhang, L. J. Song, S. Miao and J. H. Yu, *Adv. Sci.*, 2019, **6**, 1802350.

